

Multilevel, hybrid regularization method for reconstruction of fluorescent molecular tomography

Huangjian Yi,¹ Duofang Chen,¹ Xiaochao Qu,¹ Kuan Peng,¹ Xueli Chen,¹ Yuanyuan Zhou,¹ Jie Tian,^{1,2} and Jimin Liang^{1,*}

¹Life Sciences Research Center, School of Life Sciences and Technology, Xidian University, Xi'an, Shaanxi 710071, China

²Institute of Automation, Chinese Academy of Sciences, Beijing 100190, China

*Corresponding author: jimleung@mail.xidian.edu.cn

Received 1 September 2011; revised 16 November 2011; accepted 19 November 2011; posted 28 November 2011 (Doc. ID 153928); published 1 March 2012

In this paper, a multilevel, hybrid regularization method is presented for fluorescent molecular tomography (FMT) based on the *hp*-finite element method (*hp*-FEM) with a continuous wave. The hybrid regularization method combines sparsity regularization and Landweber iterative regularization to improve the stability of the solution of the ill-posed inverse problem. In the first coarse mesh level, considering the fact that the fluorescent probes are sparsely distributed in the entire reconstruction region in most FMT applications, the sparse regularization method is employed to take full advantage of this sparsity. In the subsequent refined mesh levels, since the reconstruction region is reduced and the initial value of the unknown parameters is provided from the previous mesh, these mesh levels seem to be different from the first level. As a result, the Landweber iterative regularization method is applied for reconstruction. Simulation experiments on a 3D digital mouse atlas and physical experiments on a phantom are conducted to evaluate the performance of our method. The reconstructed results show the potential and feasibility of the proposed approach. © 2012 Optical Society of America

OCIS codes: 170.3010, 170.0170, 170.6960, 170.6280.

1. Introduction

In recent years, there has been increasing interest in *in vivo* small animal optical molecular imaging due to its high molecular specificity, nonionizing radiation, and cost-effectiveness [1,2]. FMT, as a promising optical molecular imaging technique, can be applied to drug discovery and preclinical oncological research [3–5]. In this imaging process, the excitation light illuminates the tissue surface of the small animal labeled beforehand with fluorescent probes. Then, these fluorescent probes are excited to emit photons, which are measured on the surface of the small

animals. With the measured data, we can reconstruct the spatial distribution and concentration of the fluorescent probes [6,7].

One of the major challenges in reconstruction of FMT is its severe ill-posedness because only the surface data is measurable [8]. This can be alleviated by increasing the measured datasets [9], and employing the adaptive finite element method or adaptive meshing techniques [7,10,11]. In the past few years, the adaptive finite element method has been applied to FMT. In [10], Joshi *et al.* presented an adaptive finite element method for reconstruction with fluorescent targets in reflectance cube geometry using hexahedral elements. Song and Wang *et al.* developed a novel adaptive finite element algorithm based

on the longest refinement method for free-space fluorescent tomography [7]. In [11], Lv *et al.* proposed a parallel adaptive finite element method for frequency domain fluorescence molecular imaging with simplified spherical harmonics approximation in a micro-MRI-based mouse volume model. To stabilize the solution of the inverse problem, the Tikhonov regularization method is often utilized to constrain this problem since it is simple and can be solved efficiently using standard minimization methods [12,13]. However, the solution is often oversmoothed. In addition, *a priori* information is included to improve the quality of the reconstructed image, such as imposing a permissible region of the target [14]. For many FMT applications, the fluorescent target is often sparsely distributed in the reconstruction region. This can be considered as important *a priori* information for FMT. To fully take advantage of sparsity of the fluorescent target, sparsity regularization was applied to FMT reconstruction and showed good performance [15].

In this paper, we developed a multilevel, hybrid regularization strategy that combined sparsity regularization and Landweber iterative regularization for FMT reconstruction based on the *hp*-finite element method (*hp*-FEM). In the proposed approach, adaptive *hp*-FEM was employed to create a multilevel finite element mesh by autoadapted reduction of the mesh size and increment of the basis function order in the reconstruction region [16,17]. The reconstruction region was reduced from a coarse mesh to a fine mesh due to the fact that the region was comprised of nodes with large values, which is usually considered as the permissible region for the location of the fluorescent target. In the first coarse mesh, considering the region of the fluorescent target is often very small compared with the entire reconstruction region, the sparsity regularization method was employed to find a solution that provided a good initial guess and good localization for the fluorescent target. In the subsequent refined mesh levels, the reconstruction region was largely reduced because it only included nodes with large values. The fluorescent target distribution then seemed to not have obvious sparseness compared with the reduced reconstruction region, which makes these mesh levels different from the first mesh. The Landweber iterative regularization method was then performed for reconstruction. Landweber iterative regularization has been widely used for ill-posed problems because of its stability and computation efficiency [18–20]. The proposed algorithm was tested on a 3D digital mouse atlas and homogeneous physical phantom. Reconstructed results revealed the feasibility and potential of the algorithm for FMT.

The paper is organized as follows. The proposed algorithm and experimental setup are presented in Section 2. In Section 3, 3D digital mouse model simulations and physical experiments are conducted to evaluate our algorithm. We discuss the results and present a conclusion in Section 4.

2. Method

A. Linear Relationship Establishment

When FMT is excited by a continuous-wave (CW) point source, the photons' propagation is usually represented using the following coupled diffusion equations (DEs) [21–23]:

$$\begin{cases} \nabla \cdot (D_x(r) \nabla \Phi_x(r)) - \mu_{ax}(r) \Phi_x(r) = -\Theta \delta(r - r_s) \\ \nabla \cdot (D_m(r) \nabla \Phi_m(r)) - \mu_{am}(r) \Phi_m(r) = -\Phi_x(r) \eta \mu_{af}(r) \end{cases} \quad (r \in \Omega), \quad (1)$$

where subscript x and m denote excitation light and emission light, respectively. D is the diffusion coefficient, and μ_a is the absorption coefficient. Φ denotes the photon density. $\eta \mu_{af}(r)$ is the fluorescent yield to be reconstructed, which is denoted as $X(r)$ in the following part of this article. The absorption coefficient due to the fluorophore, μ_{af} , is directly related to the fluorophore concentration by the formula $\mu_{af} = \ln(10) \epsilon N$, where ϵ is the molar extinction coefficient and N is the concentration of the fluorophore [24]. Here, the Robin-type boundary conditions are implemented on the boundary [25]. Using the finite element method, for total S excitation point sources, we have the final weighted matrix:

$$\Phi_m = AX. \quad (2)$$

This is a linear relationship between the measured photon flux density and the unknown fluorescent yield. Detail descriptions are presented in [15,23].

B. Multilevel, Hybrid Regularization Method

Reconstruction of FMT is often an ill-posed inverse problem. As mentioned above, the adaptive finite element method can reduce the ill-posedness and improve the resolution of the images. A proper regularization method should consider *a priori* information of the inverse problem. We developed a multilevel, hybrid regularization method to constrain FMT reconstruction based on the *hp*-FEM. This method combines sparsity regularization and Landweber iterative regularization, which just fully considers the different *priori* information in different mesh levels.

Here, the *hp*-FEM is employed to create a multilevel mesh. In the first mesh, the reconstruction region is discretized into a uniformly coarse mesh. The region of the fluorescent target is much smaller than the reconstruction region, as shown in Fig. 1(a), hence the sparsity regularization method was applied to fully take advantage of the sparseness, which was an important *priori* information of fluorescent target. As a result, (2) can be solved by the following minimization problem with the l_1 regularization term:

$$\min_X \{ \|AX - \Phi_m\|_2^2 + \lambda_1 \|X\|_1 \}, \quad (3)$$

where $\|X\|_1 = \sum_i |x_i|$ and λ_1 is the regularization parameter. From the results in the coarse mesh, the region comprised of nodes with large values is usually considered as the permissible region for the fluorescent target. According to this point, the reconstruction region is reduced from a coarse mesh to a fine mesh. In the subsequent refined mesh levels, the reconstruction region is largely reduced and the fluorescent target distribution lacks obvious sparseness compared with the reduced reconstruction region, as shown in Figs. 1(b) and 1(c). In addition, the reconstructed results from the previous mesh provide an initial guess for fluorescent target distribution. These allow the subsequent mesh levels to be different from the first level. The Landweber iterative regularization is then performed for reconstruction. Landweber iterative regularization has been widely used for ill-posed problems because of its stability and computation efficiency [18,19]. Its form is as follows:

$$X^{\text{iter}+1} = (I - \lambda_2 A^T A) X^{\text{iter}} + \lambda_2 A^T \Phi_m, \quad (4)$$

where $\lambda_2 = 1 / \sum \text{diag}(AA^T)$ [26]. When presented with a good initial value, Landweber iterative regularization can improve the quantification smoothly in a small step length between neighboring iterations.

Assume there are sequence mesh levels L_1, \dots, L_k in FEM.

Algorithm:

Step 1: $i = 1$, for the initial coarse mesh level L_1 , reconstruct the distribution of the fluorescent target X_i for the entire reconstruction region $\Omega_i = \Omega$ using sparsity regularization, i.e., solve (3).

FOR $i = 2$ to K ,

Step 2: Determine the permissible domain Ω_i of the fluorescent target distribution from the results of the coarse mesh by choosing nodes with large values.

Step 3: Implement hp -FEM on the permissible domain Ω_i to obtain a fine mesh L_i .

Step 4: Reconstruct X_i for the reconstruction region Ω_i on the refined mesh level L_i by Landweber iterative regularization, i.e., solve (4), and $i = i + 1$.

END

C. Experimental Setup

We examined the localization and quantification abilities of the proposed reconstruction algorithm on a noncontact system. Figure 2 shows the prototype FMT imaging system. The target was placed on a rotational stage, which was controlled by the computer. Illumination was provided by a 671 nm CW laser source (CrystaLaser, Reno, Nevada, USA, and Model NO. CL671-050-O) with a power of 3 mW. The laser was a stabilized compact red laser. The spot diameter of the laser beam was approximately 0.85 mm. A custom-made 35 nm bandpass filter (HZXD, Beijing, China) centered at 720 nm was used to allow light transmission at the emission wavelength. A highly sensitive charge-coupled device (CCD) camera (Princeton Instruments PIXIS 2048B, Roper scientific, Trenton, New Jersey), which was cooled to -70°C , was employed to collect fluorescent signals. A Nikon Micro-NIKKOR 55 mm $f/2.8$ manual focus lens was mounted on the CCD camera. The laser light entered an optical scanner (RAYLASE, Germany) which consists of two mirrors. These mirrors were controlled by an in-house developed software and the laser beam can be directed at any position. When rotating the target to different angles, multiple measurements could be implemented.

3. Experiments and Results

In this section, four groups of verification experiments were designed and conducted to validate the potential and feasibility of the proposed multilevel, hybrid regularization method for FMT. First, a single fluorescent target reconstruction was performed for comparison using only the sparsity regularization method at each mesh level, and it showed better performance at the location and in the fluorescent yield reconstruction. We then investigated the robustness and stability of our algorithm by considering the noise and optical parameters effect. Third, the performance of the developed method for double fluorescent targets reconstruction was tested on a 3D digital mouse. Finally, phantom experiments were conducted to further test our method.

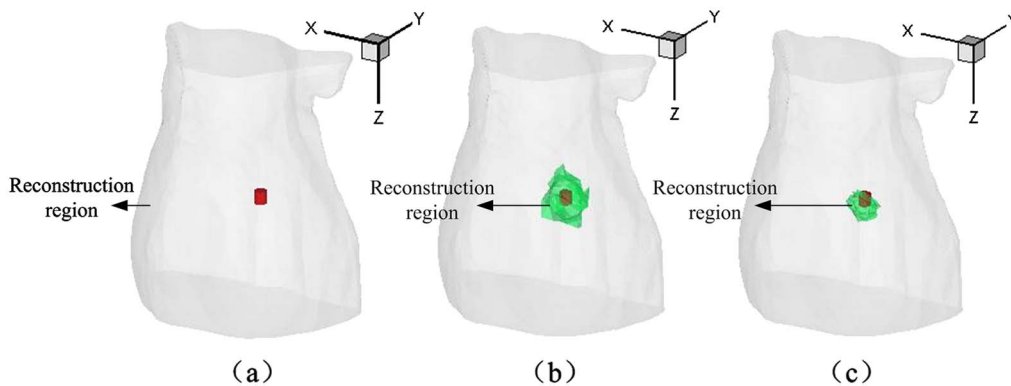


Fig. 1. (Color online) Different reconstruction regions at different mesh levels, where the red cylinder is the fluorescent target. (a) The reconstruction region for the first mesh consists of the entire mouse torso. (b) The green zone is the reconstruction region at the second level. (c) The green zone is the reconstruction region at the third level.

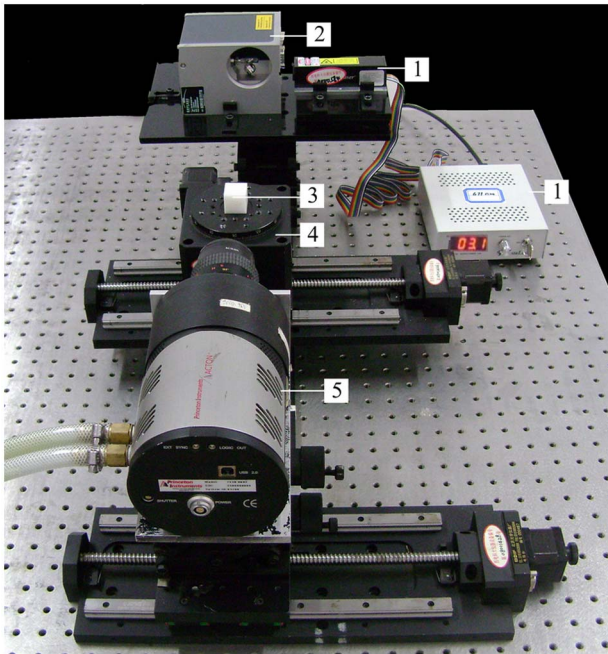


Fig. 2. (Color online) Our prototype FMT imaging system. (1) Laser, (2) optical scanner, (3) phantom, (4) rotational stage, (5) CCD camera. The components of the system are shown as described in Subsection 2.C.

A. 3D Digital Mouse Simulations for a Single Fluorescent Target

In the numerical simulations, a 3D digital mouse atlas of CT and cryosection data was utilized to provide anatomical information [27]. Only the torso section of the mouse with a height of 35 mm was selected as the region to be investigated. A cylindrical fluorescent target with a 0.8 mm radius and 1.6 mm height was placed in the liver with center at (11.9 mm, 6.4 mm, 16.4 mm), as shown in Fig. 3(a), and the fluorescent yield of the fluorescent target was set to be 0.05 mm^{-1} . For the forward problem, the torso model was discretized into 132,202 tetrahedral elements and 24,906 nodes to obtain synthetic measurements on the surface using the FEM method. The optical parameters for different organs are listed in Table 1 [14,28]. In this experiment, the fluorescent target was excited by 18 point sources at different positions in sequence, as shown in Fig. 3(b). The black dots represent positions of the excitation point sources, which were modeled as isotropic point sources located one mean free path of photon transport beneath the surface on the $z = 16.5 \text{ mm}$ plane. For each excitation source, the surface data on the opposite side with a 120° field of view (FOV) were measurable. Measurements were obtained every 20° and a total of 18 datasets were assembled for the reconstruction of the fluorescent yield.

For the inverse problem, reconstruction was conducted on a personal computer with a 2.66 GHz Intel(R) Xeon(R) CPU E5430 and 8.00 GB RAM. The maximum mesh level was set to $L_{\max} = 3$ in this paper. The digital mouse model was initially discretized

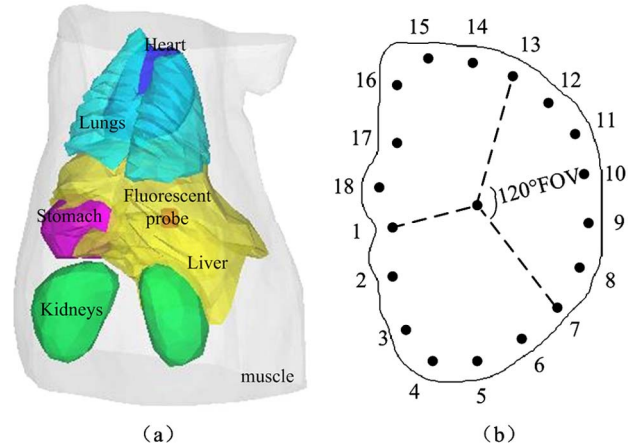


Fig. 3. (Color online) (a) Torso of the mouse atlas model with a cylindrical fluorescent target in the liver, (b) the plane of excitation sources at $z = 16.5 \text{ mm}$. The black points in (b) represent the location of the isotropic point sources. For each excitation source, fluorescence is detected at the opposite side with a 120° FOV.

into 15,141 tetrahedral elements and 3050 nodes as the coarse mesh, and the *ultima* refined mesh in the *hp*-FEM has 20,117 tetrahedral elements and 3909 nodes. Here, we employed the incomplete variables truncated conjugate gradient method as the sparsity regularization method for the first mesh [29]. We did not represent how to determine a good regularization parameter in detail since it is a very challenging task. Instead, we selected the range between $1e-8$ and $1e-13$, which is sufficient for our experiments. In order to demonstrate better performance of the presented algorithm, we compared it to use the sparsity regularization method at each mesh level. In all experiments, we selected the largest value of $X(r)$ as the reconstructed fluorescent yield, and chose the node with the largest reconstructed value as the center of the fluorescent target and the nodes with the reconstructed value bigger than 70% of the largest value as the reconstructed target. Figure 4 shows the reconstructed results at each mesh level on the axial slice where the center of the real fluorescent target is located. The figures in the left column present the results of our method, while the figures in the right column show the results of using the sparsity regularization method. The black circles in Fig. 4 denote the real fluorescent target and the color bar is the value of the fluorescent yield with a unit of mm^{-1} . The minimum value in the color bar is set to zero while the maximum one is using the larger value

Table 1. Optical Parameters of the Mouse Organs

Tissue	$\mu_{ax} (\text{mm}^{-1})$	$\mu'_{sx} (\text{mm}^{-1})$	$\mu_{am} (\text{mm}^{-1})$	$\mu'_{sm} (\text{mm}^{-1})$
Muscle	0.0052	1.08	0.0068	1.03
Heart	0.0083	1.01	0.0104	0.99
Lungs	0.0133	1.97	0.0203	1.95
Liver	0.0329	0.70	0.0176	0.65
Kidneys	0.0660	2.25	0.0380	2.02
Stomach	0.0114	1.74	0.0070	1.36

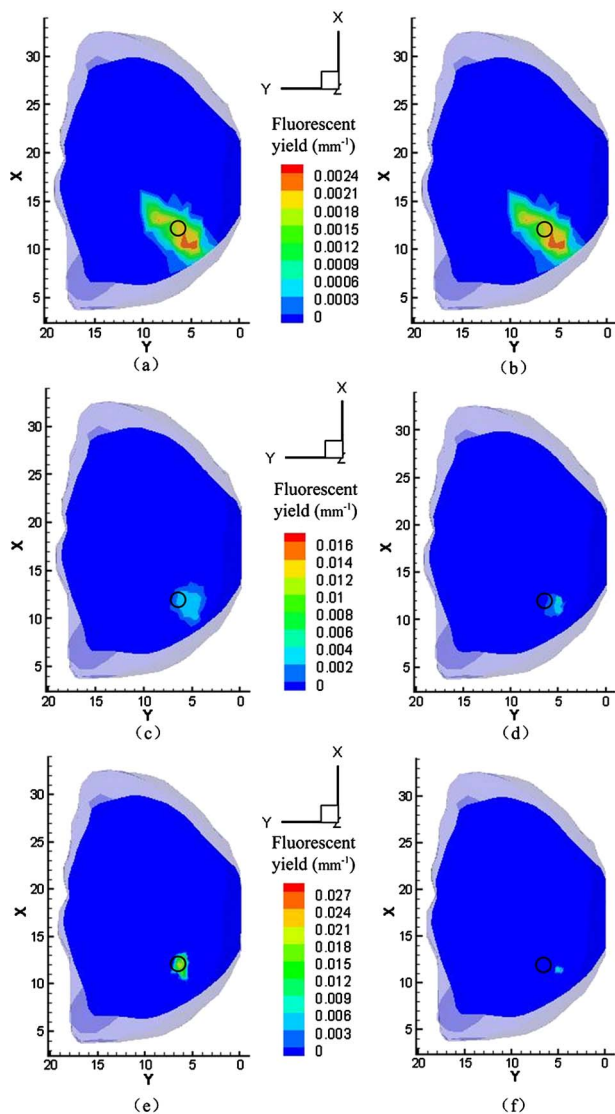


Fig. 4. (Color online) A comparison of the reconstruction results for a single fluorescent target between our method and by only using the sparsity regularization method at each mesh level. (a), (c), (e) are the transverse views of the reconstruction at $z = 16.4$ mm plane using the proposed method at the initial coarse mesh, refined mesh, and final mesh, respectively, with a threshold of 70% of the maximum value (the black circles denote the real target). (b), (d), (f) are corresponding results only using the sparsity regularization at each mesh.

of the results of two methods. To analyze the results quantitatively, Table 2 summarizes the final results and location error (LE), which is the Euclidean distance between the centers of the reconstructed and the actual target, namely $LE = [(x - x_0)^2 + (y - y_0)^2 + (z - z_0)^2]^{1/2}$, where (x, y, z) is the reconstructed coordinate and (x_0, y_0, z_0) is the actual coordinate.

Although Table 2 indicates that the reconstructed fluorescence yield of our method is similar with that of the sparsity regularization method, the maximum value location of the reconstructed target of our method is obviously more accurate than that of the compared method. As a result, the reconstructed fluorescent yield of our method on the selected slice is brighter than that of the compared method, as shown in Figs. 4(e) and 4(f).

In order to evaluate the proposed multilevel, hybrid regularization technique for reconstruction, sparsity regularization and Landweber iterative regularization were both implemented for the conventional finite element, respectively, namely on the fixed mesh. The fluorescent target is the same as described above. And the fixed mesh is also the same as the final refined mesh in our method. Table 3 and Fig. 5 provide the results. It is clear that the reconstructed positions are near to the mouse surface due to the ill-posed nature of the inverse problem. And the reconstructed fluorescent yields are much smaller than our method.

B. Stability Analysis

We evaluated the stability and robustness of the reconstruction algorithm by taking into consideration the influence of noise and optical properties. First, simulations were conducted on a 3D digital mouse by considering the measured data at different levels (0%, 10%, 20%, and 40%) of the additive Gaussian noise. Detail descriptions about this can be found in [17]. Figure 6 shows the corresponding results in transverse views on the $z = 16.4$ mm plane at each noise level. From (a), (b), (c), and (d) in Fig. 6, as the noise level increases, the reconstructed location error is kept invariable, and the fluorescent yield contains miniscule fluctuation. It demonstrates that the influence of noise on the reconstruction results is small and confirms the robustness of the proposed method.

We also investigated the dependence of the reconstruction results on the optical parameters. Two typical sets of optical properties were considered here, as listed in Table 4 and Table 5. The first set is the optical parameters at the excitation and emission wavelength of Cy5.5, i.e., wavelengths at 670 and 710 nm. The simulation, which was carried out with these optical parameters, is denoted as case 1. The second set is the optical parameters at the excitation and emission wavelength of Indocyanine green, i.e., wavelengths at 780 and 830 nm. The simulation, which was carried out with the second set of optical parameters, is denoted as case 2. All of the optical parameters were estimated according to the method

Table 2. Reconstructed Results for a Single Target on the Final Mesh

Method	Actual Position Center (mm)	Recon. Position Center (mm)	LE (mm)	Actual Fluo. Yield (mm^{-1})	Recon. Fluo. Yield (mm^{-1})
Our method	(11.9, 6.4, 16.4)	(12.2, 6.5, 16.5)	0.33	0.05	0.023
Compared method	(11.9, 6.4, 16.4)	(11.5, 5.6, 17.9)	1.75	0.05	0.027

Table 3. Quantitative Comparison Between Sparsity Regularization and Landweber Iterative Regularization Based on a Fixed Mesh

Method	Actual Position Center (mm)	Recon. Position Center (mm)	LE (mm)	Actual Fluo. Yield (mm^{-1})	Recon. Fluo. Yield (mm^{-1})
Sparsity	(11.9, 6.4, 16.4)	(9.7, 5.1, 15.7)	2.65	0.05	0.012
Landweber	(11.9, 6.4, 16.4)	(10.4, 4.0, 15.8)	2.89	0.05	0.002

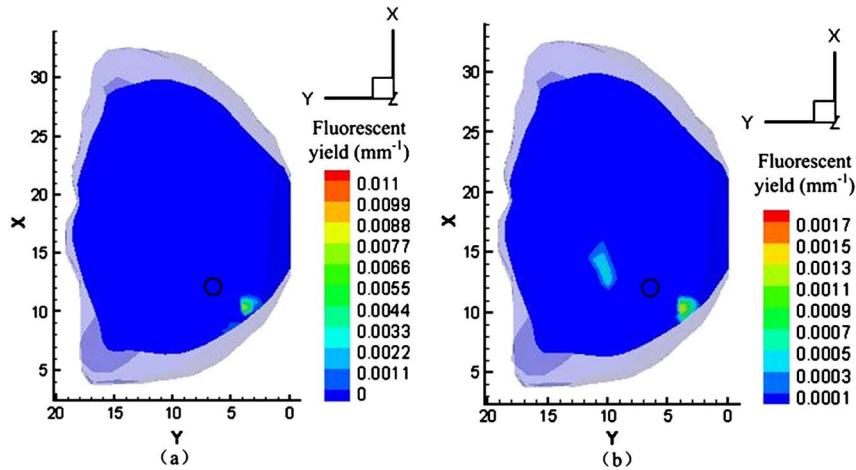


Fig. 5. (Color online) The transverse view of the reconstructed results for a single target at $z = 16.4$ mm plane, based on a fixed mesh, which is the same as the final mesh in our method. (a) The sparsity regularization method. (b) The Landweber iterative regularization.

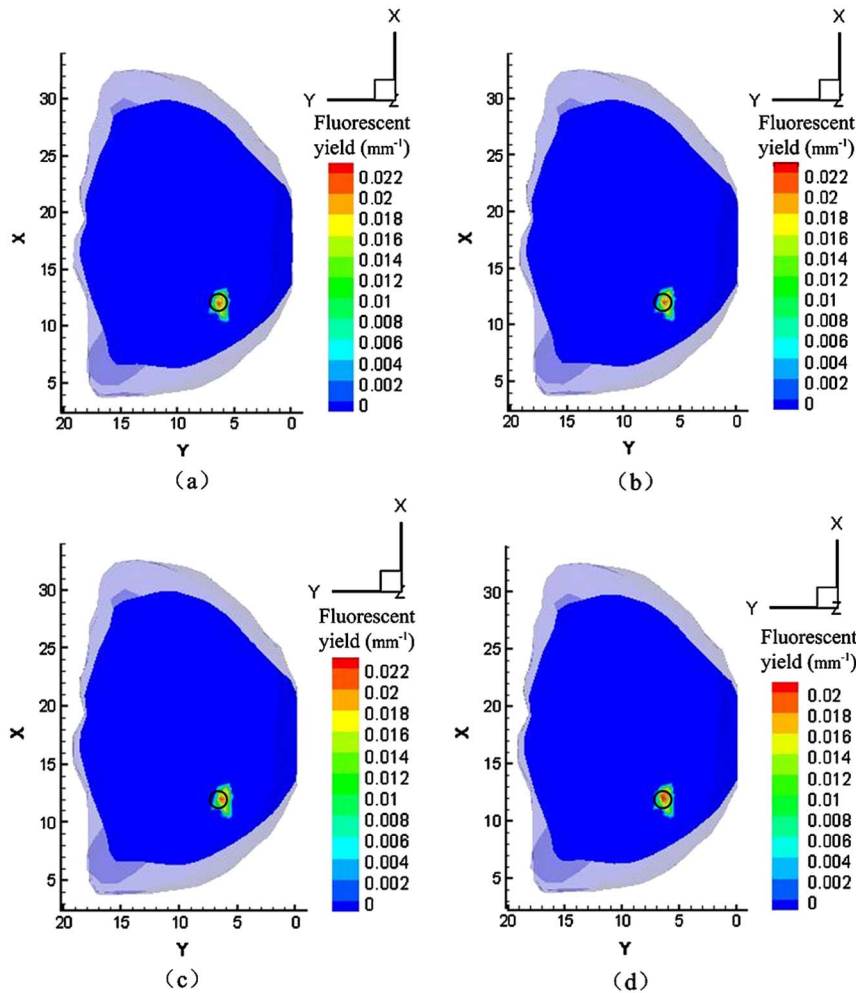


Fig. 6. (Color online) (a), (b), (c), and (d) are results for single target of the transverse views at the $z = 16.4$ mm plane using our method with 0%, 10%, 20%, and 40% of the Gaussian noise, respectively, where the black circles denote the real target.

Table 4. Optical Parameters of the Mouse Organs at 670 nm and 710 nm

	670 nm			710 nm		
	μ_{ax} (mm ⁻¹)	μ'_{sx} (mm ⁻¹)	μ'_{sx}/μ_{ax}	μ_{am} (mm ⁻¹)	μ'_{sm} (mm ⁻¹)	μ'_{sm}/μ_{ax}
Muscle	0.075	0.412	5.49	0.043	0.350	8.14
Heart	0.051	0.944	18.51	0.030	0.870	29.00
Lungs	0.170	2.157	12.69	0.097	2.093	21.58
Liver	0.304	0.668	2.20	0.176	0.629	3.57
Kidneys	0.058	2.204	38.00	0.034	2.021	59.44
Stomach	0.010	1.417	141.70	0.007	1.340	191.43

Table 5. Optical Parameters of the Mouse Organs at 780 nm and 830 nm

	780 nm			830 nm		
	μ_{ax} (mm ⁻¹)	μ'_{sx} (mm ⁻¹)	μ'_{sx}/μ_{ax}	μ_{am} (mm ⁻¹)	μ'_{sm} (mm ⁻¹)	μ'_{sm}/μ_{ax}
Muscle	0.038	0.280	7.37	0.028	0.235	8.39
Heart	0.027	0.776	28.74	0.021	0.710	33.80
Lungs	0.083	2.006	24.17	0.060	1.941	32.35
Liver	0.160	0.578	3.61	0.124	0.542	4.37
Kidneys	0.030	1.791	59.70	0.023	1.631	70.91
Stomach	0.0053	1.240	233.93	0.0043	1.167	271.40

Table 6. Quantitative Comparison Between the Two Sets of Optical Properties

Optical Parameters	Actual Position Center (mm)	Recon. Position Center (mm)	LE (mm)	Actual Fluo. Yield (mm ⁻¹)	Recon. Fluo. Yield (mm ⁻¹)
Case 1	(11.9, 6.4, 16.4)	(11.4, 6.6, 16.2)	0.57	0.05	0.024
Case 2	(11.9, 6.4, 16.4)	(12.2, 6.7, 16.5)	0.44	0.05	0.018

in [28]. The simulations were performed on the same model as that in the single target case. The reconstruction results are shown in Fig. 7. The location error and reconstructed fluorescent yield of these simulations are presented in Table 6. We can observe that the reconstructed location in case 2 is superior to that in case 1 although its fluorescent yield is a little smaller. It is noted that the ratio of the reduced scattering coefficient to the absorption coefficient in case

2 is larger than that in case 1, which means case 2 better satisfies the hypothesis of the DE model, i.e., scattering predominates over absorption.

C. Reconstruction of Double Fluorescent Targets

We also investigated the double fluorescent targets experiment with the mouse model. Two fluorescent targets were located in the liver with centers at (11.9, 6.4, 16.4 mm) and (11.9, 10.9, 16.4 mm),

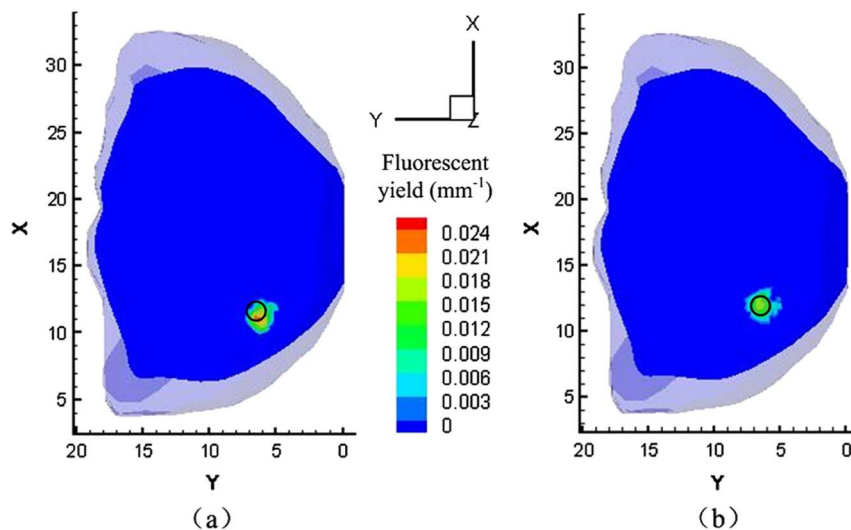


Fig. 7. (Color online) Reconstruction comparisons between two sets of optical parameters at $z = 16.4$ mm. (a) The transverse view of the result of the optical parameters in case 1. (b) The transverse view of the result of the optical parameters in case 2. The black circles represent the real target.

respectively. The initial mesh and the fluorescent yield were the same as the single target case. The final refined mesh for double fluorescent targets consists of 21,482 tetrahedral elements and 4148 nodes. The reconstructed results for each mesh are presented in Fig. 8. Table 7 gives the quantitative

results for the third mesh. In the *ultima* mesh, the two targets could be resolved clearly, although their center positions are not centered.

In addition, a group of experiments, which were performed on two targets with different separated distances (4, 3, 2.5, 2 mm), were implemented to

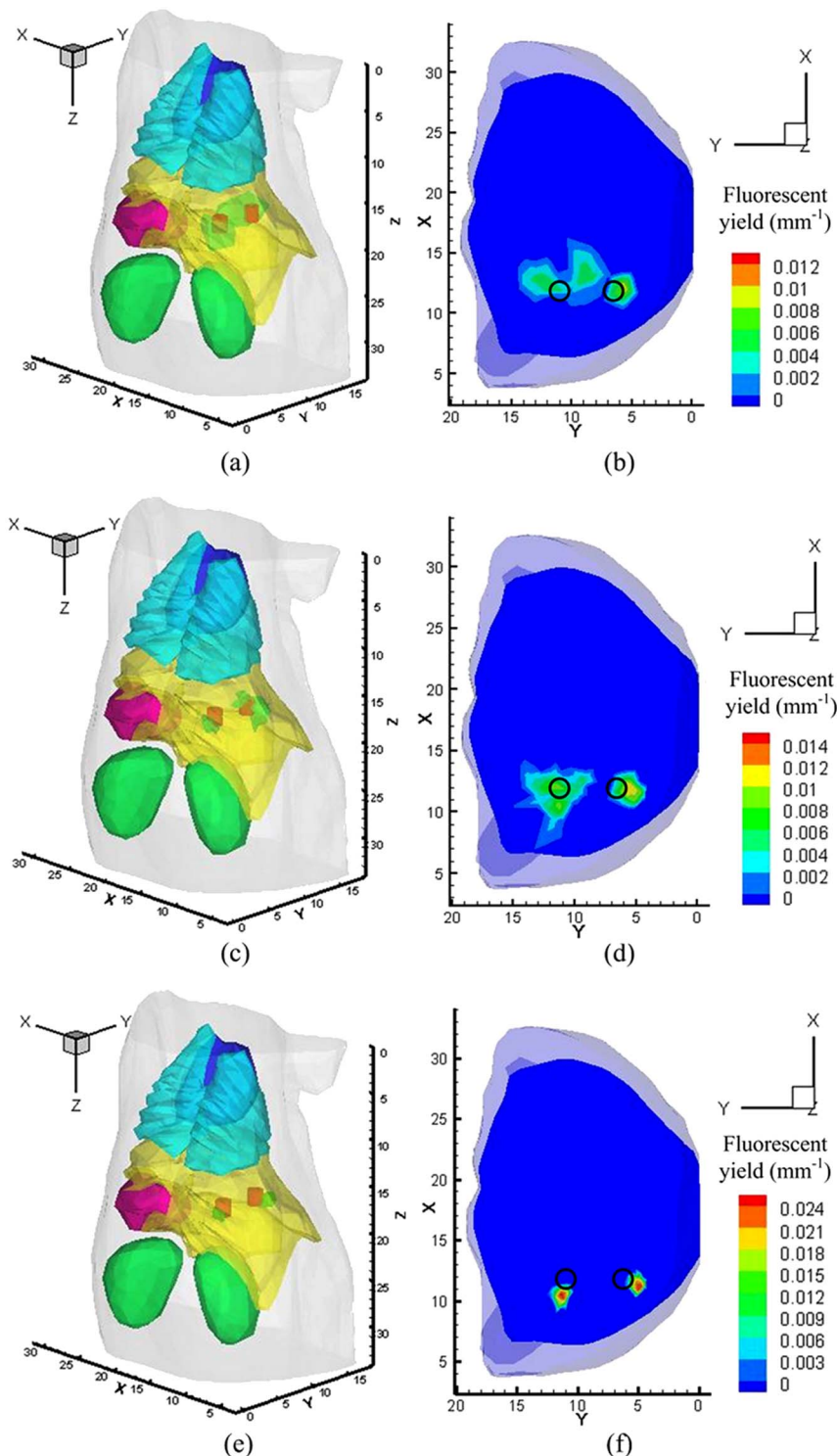


Fig. 8. (Color online) Reconstruction results for double fluorescent targets embedded in the liver using our method. (a) The isosurface view of the results from the initial coarse mesh with node values greater than 70% of the maximum value. (b) Transverse view of the reconstruction at $z = 16.5$ mm in the same mesh, where the black circle represents the real fluorescent target. (c) and (d) are the results of the refined, second level mesh. (e) and (f) are the final results of the third level mesh.

Table 7. Quantitative Results of Our Method for Double Targets on Final Mesh

Fluorescent Target	Actual Position Center (mm)	Recon. Position Center (mm)	LE (mm)	Actual Fluo. Yield (mm^{-1})	Recon. Fluo. Yield (mm^{-1})
Target 1	(11.9, 10.9, 16.4)	(10.4, 11.6, 16.7)	1.68	0.05	0.024
Target 2	(11.9, 6.4, 16.4)	(11.2, 4.8, 16.6)	1.76	0.05	0.026

further demonstrate the validity of the algorithm. Figure 9 shows the reconstructed results on the axial slice where the center of the real fluorescent targets were located. Figures 9(a), 9(b), 9(c), and 9(d) represent the reconstructed results for the distances of 4, 3, 2.5, and 2 mm, respectively. It is obvious that our method can discriminate two targets with the separated distances of 4, 3, 2.5 mm. In Fig. 9(d), the reconstructed two targets become one target, namely our method cannot discriminate these two targets when the separated distance is smaller than 2 mm. It indicates that our method is able to discriminate two targets 2.5 mm apart.

D. Physical Experiments

Physical experiments were also conducted to further evaluate the proposed algorithm. In our physical experiment, a cubic phantom was utilized with a side length of 20 mm, which is shown in Fig. 10(a). The

phantom was made from polyoxymethylene. The optical parameters for both excitation and emission wavelengths are illustrated in Table 8 [15]. A small hole with a 1 mm radius was drilled to emplace the 4000 nM Cy5.5 solution (with the extinction coefficient of about $0.019 \text{ mm}^{-1} \mu\text{M}^{-1}$ and the quantum efficiency of 0.23 at the peak excitation wavelength of 671 nm [30]), which was used as the fluorescent target. The center of the hole was at (16, 8, 9.5 mm) with a 2 mm height, as shown in Fig. 10(b). The fluorescent target was excited by point sources from four different positions at the $z = 10 \text{ mm}$ plane, and CCD acquired data at four different views are shown in Fig. 10(c).

In the experiment, the cubic phantom was discretized into 14,780 tetrahedral elements and 2989 nodes for the coarse mesh during inverse reconstruction. The CCD camera was adopted to measure the signal on the phantom surface from four views by

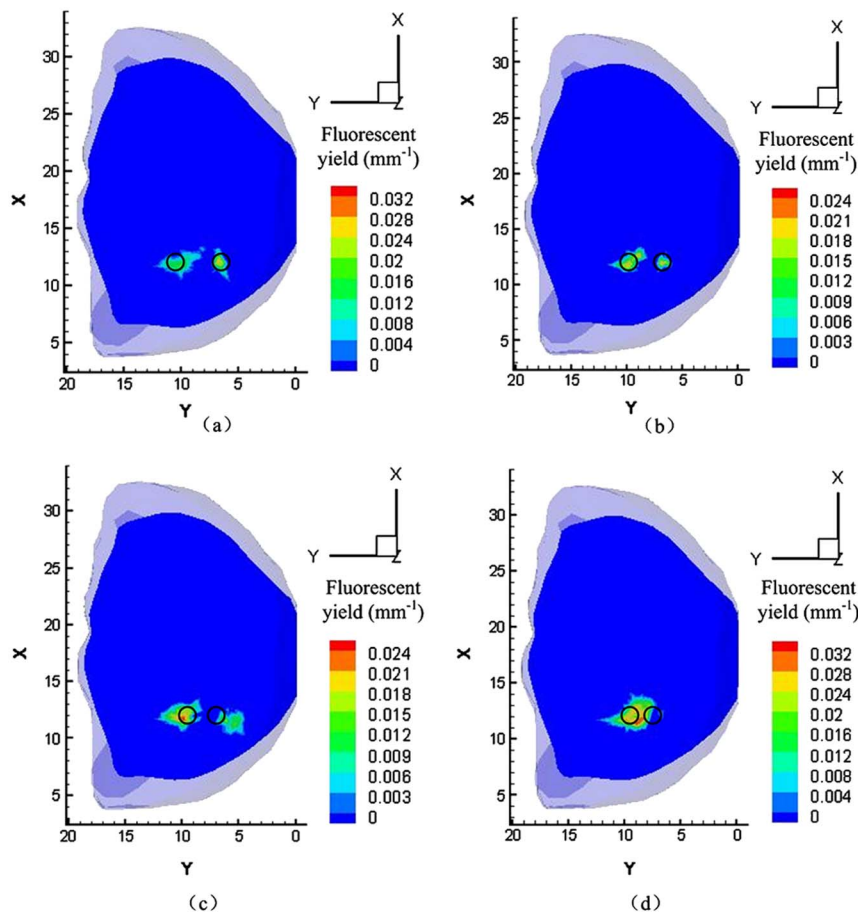


Fig. 9. (Color online) Reconstructed results for two targets with different center distances at $z = 16.4 \text{ mm}$ plane. (a), (b), (c), and (d) are the transverse views of reconstructed results using our method with center distances of 4, 3, 2.5, and 2 mm, respectively, where the black circles denote the real target.

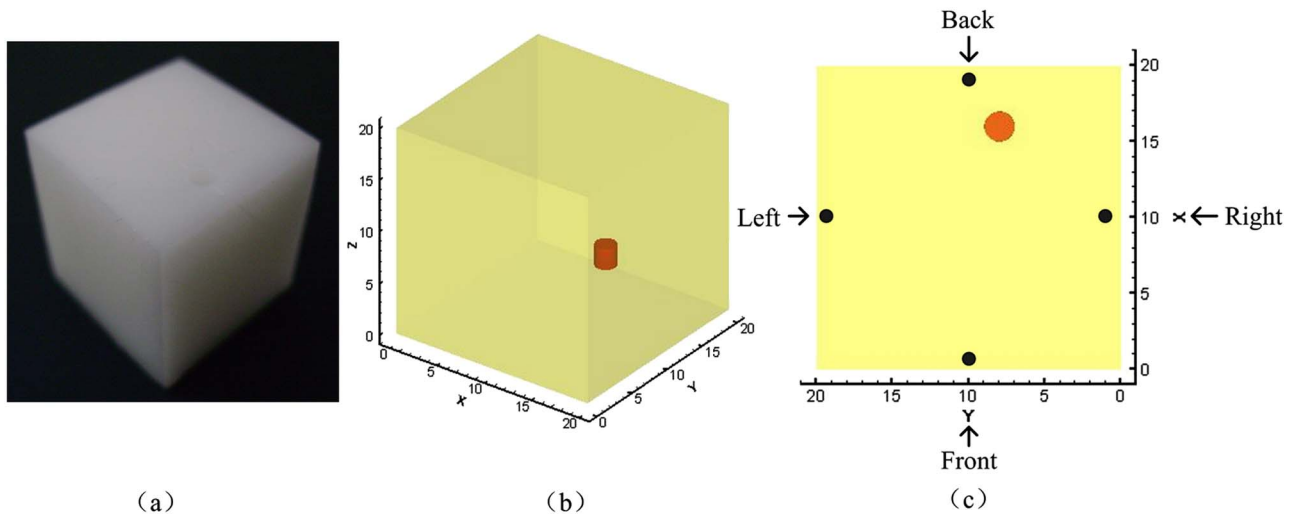


Fig. 10. (Color online) Physical phantom. (a) The homogeneous physical phantom. (b) The 3D view of the single fluorescent target in the cubic phantom. (c) The x - y view on the $z = 10$ mm plane, where the black dots represent the excitation point source positions. Four degrees show the direction of the CCD camera during data acquisition.

Table 8. Optical Parameters of the Homogeneous Cubic Phantom

Wavelength (nm)	μ_a (mm ⁻¹)	μ'_s (mm ⁻¹)
671	0.00029	1.08
710	0.00051	1.11

rotating the phantom with an angular increment of 90°. Figure 11 shows the acquired data on CCD from four views. From the measured data, we reconstructed the location of the Cy 5.5 solution using the presented algorithm. Final results are shown in Fig. 12(a) and 12(b) with reconstructed coordinate (16.8, 7.6, 9.5 mm) and location error 0.89 mm. Figure 12(a) is the isosurface view of the reconstruction with top 30% of the maximum value. The red cylinder represents the real position placed the Cy 5.5 solution, while the green zone is the reconstructed target and Fig. 12(b) is the transverse view of the reconstruction at the $z = 9.5$ mm plane. The reconstructed concentration of Cy5.5 dye is about 616.9 nM.

4. Discussion and Conclusion

We developed a multilevel, hybrid regularization technique for FMT reconstruction. This algorithm combines sparsity regularization and Landweber iterative regularization for the inverse problem based on the hp -FEM. To take full advantage of sparsity of the fluorescent target in the coarse mesh, sparsity regularization was employed to constrain this problem. In subsequently refined mesh levels, the reconstruction region was largely reduced because it was comprised of nodes with large values. In addition, results from the coarse mesh not only guide the mesh refinement, but also provide a good localization of the fluorescent target and a good initial value of the fluorescent yield. These allow subsequent mesh levels to be different from the first coarse mesh. The Landweber iterative regularization method was then utilized for FMT reconstruction, which can smoothly improve quantification in a small step length between neighboring iterations.

Both numerical simulation with a digital mouse and the physical phantom experiment were

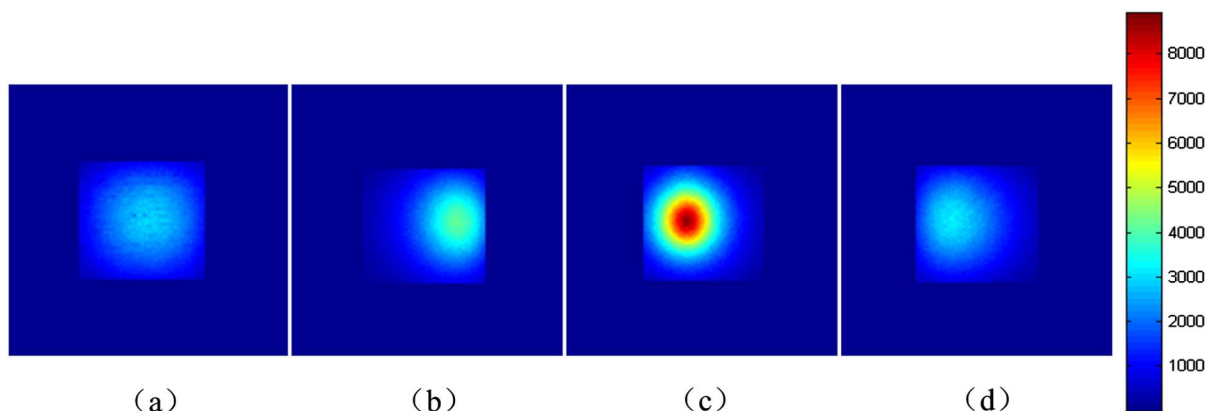


Fig. 11. (Color online) Surface data acquired by CCD from four views. (a) front view, (b) right view, (c) back view, (d) left view.

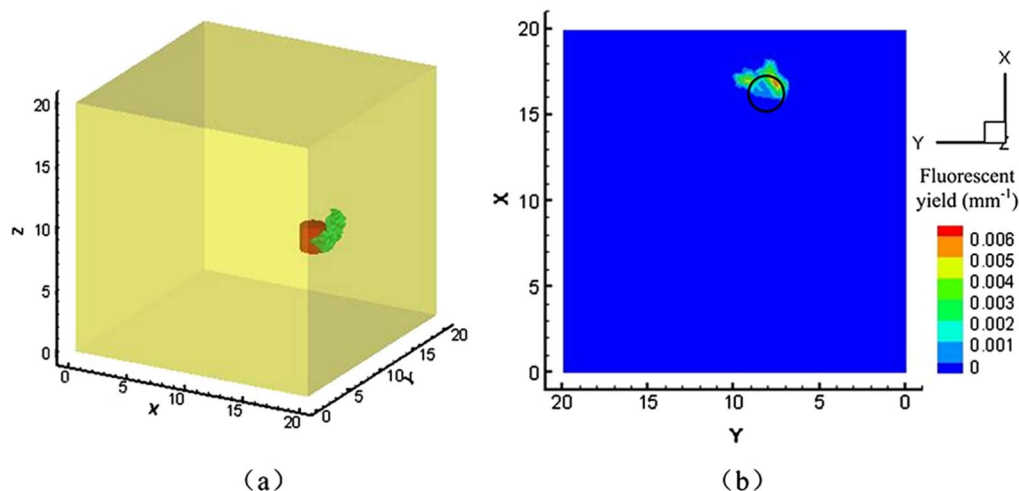


Fig. 12. (Color online) Reconstructed results of the cubic phantom with a single fluorescent target. (a) The isosurface view of the results with top 30% of the maximum value. The red cylinder is the real target while the green zone is the reconstructed target. (b) The transverse view of the reconstruction on the $z = 9.5$ mm plane. The black circle represents the real target.

conducted to evaluate the potential and feasibility of the new method. First, a simulation experiment with a single fluorescent target with heterogeneous optical properties was conducted in a digital mouse. The result from the presented method was compared to the results from using the sparsity regularization method at each mesh individually, and our method showed better performance. However, the latter method obtained a very sparse solution and its fluorescent yield was a slightly larger than our method. This may be because sparsity regularization was utilized for every mesh. To further test our method, sparsity regularization and Landweber iterative regularization were conducted on a fixed mesh, respectively. The numbers of nodes and tetrahedral elements in the fixed mesh were the same as that of the final mesh in our method. In the experiment, the sparsity regularization and Landweber iterative regularization provided location errors 2.65 and 2.89 mm, respectively, and the reconstructed fluorescent yield values were smaller than our method. In order to demonstrate the robustness of the proposed method, we considered the detected data at different levels (0%, 10%, 20%, and 40%) of the additive Gaussian noise in the same mouse model as described in the first experiment. The results indicated that as the noise level increased, the reconstructed location was kept invariable and the fluorescent yield had a minimal fluctuation. We also investigated the dependence of our target localization on the optical properties based on two typical sets of optical parameters. For double targets, our algorithm was able to discriminate two targets clearly separated at 2.5 mm distance. In the phantom experiment, a homogenous cubic phantom with a single target was studied to further evaluate the proposed algorithm. In all experiments, we have found that the values of the reconstructed fluorescent yields were smaller than the actual ones. This may be caused by the ill-posed and underdetermined nature of the inverse problem [21]. Moreover, Lin *et al.* showed that

the fluorophore concentration can be accurately recovered with a small error only when both the optical background property and structural *a priori* information were utilized [6,31,32]. The location of the fluorescent target was obtained from structural *a priori* information (from x-ray computed tomography) and used to guide FMT reconstruction together with the diffuse optical tomography (DOT) functional *a priori* information; when only the optical background property was provided by DOT, the fluorophore concentration was recovered with a large error [6]. In our experiments, we localized the fluorescent target and reconstructed the fluorescent yield simultaneously only utilizing the optical parameters of tissues as functional *a priori* information without structural *a priori* information to localize the fluorescent target. As a result, the reconstructed fluorescent yield values were smaller than the actual ones. In addition, the mesh refinement scale and the effectiveness of the optimization method may also affect the fluorescent yield reconstruction.

In conclusion, we have developed an effective method for FMT. Numerical results in the simulation experiment and physical phantom experiment both showed the feasibility and potential of the multilevel, hybrid regularization technique, especially for a single target. Our new method would be applied in *in vivo* small animal imaging. In addition, some accelerated computation strategy will be used in future studies to reduce the computation time.

The authors thank Dr. Jorge Ripoll for providing suggestions solving the problems regarding the phantom experiments. This work is supported by the Program of the National Basic Research and Development Program of China (973) under grant 2011CB707702, the National Natural Science Foundation of China (NSFC) under grants 81090272, 81101083, 81101084, 81101100, 81000632, 30900334, the Shaanxi Provincial Natural Science Foundation Research Project under grant

References

1. V. Ntziachristos, J. Ripoll, L. V. Wang, and R. Weissleder, "Looking and listening to light: the evolution of whole body photonic imaging," *Nat. Biotechnol.* **23**, 313–320 (2005).
2. J. Tian, J. Bai, X. Yan, S. Bao, Y. Li, W. Liang, and X. Yang, "Multimodality molecular imaging," *IEEE Eng. Med. Biol. Mag.* **27**, 48–57 (2008).
3. E. E. Graves, R. Weissleder, and V. Ntziachristos, "Fluorescence molecular imaging of small animal tumor models," *Curr. Mol. Med.* **4**, 419–430 (2004).
4. M. J. Niederre, R. H. de Kleine, E. Aikawa, D. G. Kirsch, R. Weissleder, and V. Ntziachristos, "Early photon tomography allows fluorescence detection of lung carcinomas and disease progression in mice in vivo," *Proc. Natl. Acad. Sci. USA* **105**, 19126–19131 (2008).
5. J. K. Willmann, N. van Bruggen, L. M. Dinkelborg, and S. S. Gambhir, "Molecular imaging in drug development," *Nat. Rev. Drug Discov.* **7**, 591–607 (2008).
6. Y. Lin, W. C. Barber, J. S. Iwanczyk, W. W. Roeck, O. Nalcioglu, and G. Gulsen, "Quantitative fluorescence tomography using a trimodality system: in vivo validation," *J. Biomed. Opt.* **15**, 040503 (2010).
7. X. Song, D. Wang, N. Chen, J. Bai, and H. Wang, "Reconstruction for free-space fluorescence tomography using a novel hybrid adaptive finite element algorithm," *Opt. Express* **15**, 18300–18317 (2007).
8. D. Han, J. Tian, K. Liu, J. Feng, B. Zhang, X. Ma, and C. Qin, "Sparsity promoting tomographic fluorescence imaging with simplified spherical harmonics approximation," *IEEE Trans. Biomed. Eng.* **57**, 2564–2567 (2010).
9. C. Li, G. S. Mitchell, J. Dutta, S. Ahn, R. M. Leahy, and S. R. Cherry, "A three-dimensional multispectral fluorescence optical tomography imaging system for small animals based on a conical mirror design," *Opt. Express* **17**, 7571–7585 (2009).
10. A. Joshi, W. Bangerth, and E. M. Sevick-Muraca, "Adaptive finite element based tomography for fluorescence optical imaging in tissue," *Opt. Express* **12**, 5402–5417 (2004).
11. Y. Lv, B. Zhu, H. Shen, J. C. Rasmussen, G. Wang, and E. M. Sevick-Muraca, "A parallel adaptive finite element simplified spherical harmonics approximation solver for frequency domain fluorescence molecular imaging," *Phys. Med. Biol.* **55**, 4625–4645 (2010).
12. A. D. Zacharopoulos, P. Svenmarker, J. Axelsson, M. Schweiger, S. R. Arridge, and S. Andersson-Engels, "A matrix-free algorithm for multiple wavelength fluorescence tomography," *Opt. Express* **17**, 3025–3035 (2009).
13. X. Zhang, C. T. Badea, and G. A. Johnson, "Three-dimensional reconstruction in free-space whole-body fluorescence tomography of mice using optically reconstructed surface and atlas anatomy," *J. Biomed. Opt.* **14**, 064010 (2009).
14. A. Cong and G. Wang, "A finite-element-based reconstruction method for 3D fluorescence tomography," *Opt. Express* **13**, 9847–9857 (2005).
15. D. Han, J. Tian, S. Zhu, J. Feng, C. Qin, B. Zhang, and X. Yang, "A fast reconstruction algorithm for fluorescence molecular tomography with sparsity regularization," *Opt. Express* **18**, 8630–8646 (2010).
16. M. Ainsworth and B. Senior, "Aspects of an adaptive hp-finite element method: Adaptive strategy conforming approximation and efficient solvers," *Comput. Methods Appl. M* **150**, 65–87 (1997).
17. R. Han, J. Liang, X. Qu, Y. Hou, N. Ren, J. Mao, and J. Tian, "A source reconstruction algorithm based on adaptive hp-FEM for bioluminescence tomography," *Opt. Express* **17**, 14481–14494 (2009).
18. L. Landweber, "An iteration formula for Fredholm integral equations of the first kind," *Am. J. Math.* **73**, 615–624 (1951).
19. R. Ramlau, "A modified Landweber method for inverse problems," *Numer. Funct. Anal. Optim.* **20**, 79–98 (1999).
20. J. Liu, *Regularization Methods to Ill-Posed Problem and Its Applications* (Science Press, 2005).
21. S. R. Arridge, "Optical tomography in medical imaging," *Inverse Probl.* **15**, R41–R93 (1999).
22. Y. Tan and H. Jiang, "DOT guided fluorescence molecular tomography of arbitrarily shaped objects," *Med. Phys.* **35**, 5703–5707 (2008).
23. D. Wang, X. Liu, Y. Chen, and J. Bai, "A novel finite-element-based algorithm for fluorescence molecular tomography of heterogeneous media," *IEEE Trans. Inf. Technol. Biomed.* **13**, 766–773 (2009).
24. M. A. Naser and M. S. Patterson, "Improved bioluminescence and fluorescence reconstruction algorithms using diffuse optical tomography, normalized data, and optimized selection of the permissible source region," *Biomed. Opt. Express* **2**, 169–184 (2011).
25. M. Schweiger, S. R. Arridge, M. Hiraoka, and D. T. Delpy, "The finite element method for the propagation of light in scattering media: Boundary and source conditions," *Med. Phys.* **22**, 1779–1792 (1995).
26. A. Kirsch, *An Introduction to the Mathematical Theory of Inverse Problems* (Springer-Verlag, 1996).
27. B. Dogdas, D. Stout, A. F. Chatziioannou, and R. M. Leahy, "Digimouse: a 3D whole body mouse atlas from CT and cryosection data," *Phys. Med. Biol.* **52**, 577–587 (2007).
28. G. Alexandrakakis, F. R. Rannou, and A. F. Chatziioannou, "Tomographic bioluminescence imaging by use of a combined optical-PET (OPET) system: a computer simulation feasibility study," *Phys. Med. Biol.* **50**, 4225–4241 (2005).
29. X. He, J. Liang, X. Wang, J. Yu, X. Qu, X. Wang, Y. Hou, D. Chen, F. Liu, and J. Tian, "Sparse reconstruction for quantitative bioluminescence tomography based on the incomplete variables truncated conjugate gradient method," *Opt. Express* **18**, 24825–24841 (2010).
30. F. Gao, H. J. Zhao, Y. Tanikawa, and Y. Yamada, "A linear, featured-data scheme for image reconstruction in time-domain fluorescence molecular tomography," *Opt. Express* **14**, 7109–7124 (2006).
31. Y. Lin, H. Gao, O. Nalcioglu, and G. Gulsen, "Fluorescence diffuse optical tomography with functional and anatomical a priori information: feasibility study," *Phys. Med. Biol.* **52**, 5569–5585 (2007).
32. Y. Lin, W. C. Barber, J. S. Iwanczyk, W. Roeck, O. Nalcioglu, and G. Gulsen, "Quantitative fluorescence tomography using a combined tri-modality FT/DOT/XCT system," *Opt. Express* **18**, 7835–7850 (2010).